Systematic observation of a seismic back-front during fluid injection in both natural and anthropogenic earthquake swarms

Louis de Barros, Philippe Danré, Dmitry Garagash, Frédéric Cappa, Olivier Lengliné

Earth Planet. Sci. Lett. 641 (2024) 118849

Contents lists available at ScienceDirect

Earth and Planetary Science Letters

journal homepage: www.elsevier.com/locate/epsl

Systematic observation of a seismic back-front during fluid injection in both natural and anthropogenic earthquake swarms

Louis De Barros [a,*], Philippe Danré [a], Dmitry Garagash [b], Frédéric Cappa [a], Olivier Lengliné [c]

[a] Géoazur, Observatoire de la Côte d'Azur, CNRS, IRD, Université Côte d'Azur, 250 rue Albert Einstein, Sophia Antipolis, Valbonne 06560, France
[b] Department of Civil and Resource Engineering, Dalhousie University, Halifax, Canada
[c] Institut Terre et Environnement de Strasbourg, UMR7063, Université de Strasbourg/CNRS, Strasbourg CEDEX 67084, France

ARTICLE INFO

Edited by: Dr H Thybo

Keywords:
Induced seismicity
Seismic swarms
Seismic back-front
Fluid-induced aseismic slip
Earthquake nucleation length

ABSTRACT

Seismic swarms represent clusters of seismicity without large mainshocks. While they occur naturally, they can also be induced by human activities, particularly during reservoir hydraulic stimulations. A striking feature of seismic swarms is the migration of their hypocenters. The seismic front, initially attributed to fluid diffusion, has more recently been understood as the result of the propagation of a fluid-induced aseismic slip. Close to the center of the swarm, a seismic back-front is commonly admitted after the injection end, but a low density of events is also observed during the injection period. In our investigation, based on a compilation of 22 swarms of both natural or anthropogenic origin, we aim to explore the existence and origin of a seismic back-front. Interestingly, we observe a post-injection back-front only in rare cases, where a rapid fluid pressure decrease is imposed at the injection point. Conversely, a back-front during the injection period is always observed in both types of swarms. Consequently, the back-front cannot be reliably used to infer the end of injection, as commonly done for natural swarms. Moreover, the occurrence of this back-front during injection is linked to an increase in the minimum magnitude of seismic events. We interpret the vanishing of the seismicity close to the injection point as a consequence of the increase in earthquake nucleation length with increasing fluid pressure. With a substantially enhanced capability for detecting small events, it may become feasible to use this back-front as a means of monitoring injection pressure, even in the context of natural swarms.

1. Introduction

Seismic swarms are sequences of earthquakes, clustered in space and time, characterized by the absence of a larger event at the onset (Vidale and Shearer, 2006). They occur naturally in various tectonic contexts, including mountain ranges, strike-slip domains or rifting areas (De Barros et al., 2020; Ross et al., 2020; Ruhl et al., 2016). Additionally, they can be induced by anthropogenic activities such as fluid injections for geological reservoir exploitation or wastewater disposals (Ellsworth, 2013; Foulger et al., 2018; Keranen and Weingarten, 2018). Notably, fault stimulation for Enhanced Geothermal System (EGS) can trigger seismicity including potentially damaging events (Grigoli et al., 2018). Apart from swarms that are driven by slow-slips, the similarity in behavior between natural swarms and injection-induced seismicity (Danré et al., 2022) suggests that both types of earthquake sequences are primarily induced by fluid pressure perturbation at depth.

In fluid-induced earthquake sequences, a common phenomenon is the migration of seismicity, where hypocenters progressively move away from the injection point over time. The seismic front migration was initially attributed to fluid pressure diffusion triggering seismicity by decreasing the fault normal stress (Shapiro et al., 1997; Talwani et al., 2007). However, recent models show that fluid pressure first induces an aseismic slip, which can propagate more rapidly than the fluid pressure (Bhattacharya and Viesca, 2019; Cappa et al., 2019; De Barros et al., 2021; Wynants-Morel et al., 2020). This fluid-induced aseismic slip subsequently triggers seismicity at its boundaries, forming what is observed as a seismic front. Consequently, the seismic front is indicative of the aseismic slip front, which differs from the fluid pressure front. The shape of this front thus depends on fault friction properties and stress conditions, rather than hydraulic characteristics (De Barros et al., 2021).

Within the seismic swarm, a back-front has been observed after the cessation of injection (Parotidis et al., 2004). It is defined as the boundary separating the still active seismic domain from the region closer to the injection, which becomes seismically quiescent. When the

* Corresponding author.
E-mail address: debarros@geoazur.unice.fr (L. De Barros).

https://doi.org/10.1016/j.epsl.2024.118849
Received 19 March 2024; Received in revised form 6 June 2024; Accepted 12 June 2024

injection stops, the decreasing fluid pressure results in a locking front, causing seismicity to cease as the failure criterion is no longer met (Jacquey and Viesca, 2023; Sáez and Lecampion, 2023; Segall and Lu, 2015). The Kaiser effect, which describes the absence of seismicity until previous stress level was exceeded, was also used to explain the post-injection absence of seismic events (Baisch et al., 2006; Parotidis et al., 2004). As the slip propagates away from the injection, a stress shadow may also develop at the tail of the propagating crack (Dahm et al., 2010; Segall and Lu, 2015). These various models, derived for the post-injection phase for injection-induced seismicity, have been extended to natural swarms. The observation of a back-front within a natural swarm is now commonly used to indicate the end of the fluid pressure perturbation that primarily drives the swarm (Liu et al., 2023; Mesimeri et al., 2019; Parotidis et al., 2005; Passarelli et al., 2018; Sirorattanakul et al., 2022).

However, an absence of seismic events close to the injection point was also observed during active injection periods. Examples of this phenomenon were documented during injection-induced seismicity experiments at decametric scale (De Barros et al., 2023, 2018) or during reservoir stimulations (Eyre et al., 2019). This lack of events was attributed to a predominantly aseismic deformation around the injection point. Induced seismicity resulting from EGS stimulation also disappears near the going-on injection (Martínez-Garzón et al., 2014). Similarly, several natural swarms exhibit seismicity vanishing over time at the center of swarm (De Barros et al., 2019a; Ross and Cochran, 2021; Yoshida and Hasegawa, 2018). Consequently, an additional back-front may exist even when fluid pressure supply is still active.

The aim of this study is to explore the existence of a back-front during the injection period and to infer its origin in the context of the recent models of fluid-induced aseismic slip. To achieve this, we use a comprehensive compilation of both natural swarms and fluid-induced sequences, aiming to discern if these two types of sequence share a similar behavior. By analyzing the density of seismic events and the magnitude variations, we aim to investigate the hypothesis that the observed back-front during injection can be attributed to an increase in earthquake nucleation length on asperities in close proximity to the injection.

2. Seismological data

The swarms examined in this study, from a worldwide source, are either induced by anthropogenic injections or occurring naturally. We particularly focus on swarms from EGS, where injections typically take place in isolated boreholes, resulting in swarms characterized by simple geometry (Zang et al., 2014). Moreover, EGS stimulations typically involve a single, short injection lasting less than a few weeks, with a pressure maintained at a steady level during most of this period. As a result, the induced seismic swarms do not exhibit the multiple, episodic or discontinuous seismic stages often observed during longer injection for hydrothermal reservoir exploitation or wastewater storage (Schultz et al., 2023b). EGS stimulations also occur in relatively homogeneous crystalline rocks, allowing us to neglect variability in frictional properties that leads to highly heterogeneous distributions of seismic and aseismic slip and distant seismicity, as seen in sedimentary layers during shale gas recovery (Eyre et al., 2019). Additionally, we focus on EGS-induced sequences where seismicity is primarily driven by direct fluid pressure effects (including fluid-induced aseismic slip) rather than by poroelastic deformation, which is more dominant in cases such as wastewater storage (Goebel and Brodsky, 2018). Finally, the sequences considered in this study all exhibit seismic migration that appears to originate from a single, well-defined point. The 14 EGS sequences originate from various locations, including (1) Soultz-sous-Forêts (Bourouis and Bernard, 2007; Cauchie et al., 2020; Cuenot et al., 2008; Drif et al., 2024) and Rittershoffen (Lengliné et al., 2017) in the French Rhine Graben, (2) Basel in Switzerland (Deichmann and Giardini, 2009; Herrmann et al., 2019), (3) Cooper Basin (Baisch et al., 2015, 2006) and Paralana (Albaric et al., 2014) in Australia, (4) the Utah FORGE project in the US (Whidden et al., 2023), and (5) Helsinki in Finland (Kwiatek et al., 2019). Additionally, we considered eight natural swarms from diverse contexts. In mountain ranges, swarms have been observed in the Ubaye Valley in the French Alps (Daniel et al., 2011; De Barros et al., 2019a; Jenatton et al., 2007) and the Mogul area in Nevada, US (Ruhl et al., 2016). Swarms in extensional areas were documented in the Corinth gulf in Greece (De Barros et al., 2020; Pacchiani and Lyon-Caen, 2010) and the West-Bohemia in Czech republic (Fischer et al., 2014), while the Cahuilla swarm is situated in a strike-slip area in California, US (Ross et al., 2020). Considering their migration properties, it is assumed that all these swarms are primarily driven by fluid diffusion processes (Danré et al., 2022). The durations of these swarms range from approximately 2 h to 3 years, with sizes varying from 400 m to 5 km, and maximum magnitudes between 0.1 and 3.8. A summary of the main properties and origins of these catalogs is provided in Table S1 in supplementary materials.

We exclusively used the magnitude, timing and location of seismic events. Given the diverse origins and periods of these catalogs, the quality of locations and the magnitude computation may vary. Nevertheless, we opted to use these catalogs in their original form without making adjustments.

3. A seismic back-front during fluid injection periods

A conventional approach to study earthquake migration involves examining the distance R from the injection point plotted against elapsed time T in what is called R-T plot (Shapiro et al., 1997). This projection assumes that seismic migration is globally radial, in a geometry that can go from 2D, where a single fault zone is reactivated to 3D if critically-stressed faults are homogeneously distributed. It stays valid if seismicity is dominantly migrating in a single direction. Notably, the injection point and starting time is unknown for natural swarms. To maintain consistency, we adopt the assumption that the origin is determined by the time of the first event and the median location of the initial 10 events for both types of swarms. Consequently, the origin time differs from the start of injection, representing the time when injection pressure reaches a critical level, triggering seismicity. Fig. S1 shows the distance between the spatial origin inferred from seismicity and the injection well for 11 induced sequences. These distances vary from a few meters in the 1993 Soultz-sous-Forêts injection to more than 100 m in the 2012 Cooper Basin, representing less than 15 % of the swarm size in most cases. Given the potential uncertainties in seismic absolute location, this inferred spatial origin is more consistent than the actual injection position for R-T analysis of the seismicity. Moreover, fluid pressure is often injected in open borehole section. In such cases, the spatial origin is identified as the point where faults are most critically stressed in response to the injection, thereby initiating seismic failures. For those reasons, this spatial origin is referred to as the injection point in this study.

Figs. 1, S2 and S3 show the event density computed on 30 windows in both space and time, deviating from the conventional representation of individual seismic events. The seismic front, theoretically the maximum distance reached by seismicity at each time, is defined as the 90th percentile of event numbers in distance within a sliding time window. This allows taking into account location uncertainties and events arising from background noise (Danré et al., 2022; De Barros et al., 2021; Goebel and Brodsky, 2018). Analogously, the back-front is defined as the 10th percentile of event numbers. We examine the behaviors of both fronts during the injection period and following the cessation of the fluid pressure supply (injection shut-in time) that drives the swarms. While this time is known for most anthropogenic injection-induced sequences, it remains unknown for natural swarms. In such cases, we use the time of the maximum migration distance of the front, a parameter demonstrated to be closely aligned with the injection shut-in time (Danré et al., 2023).

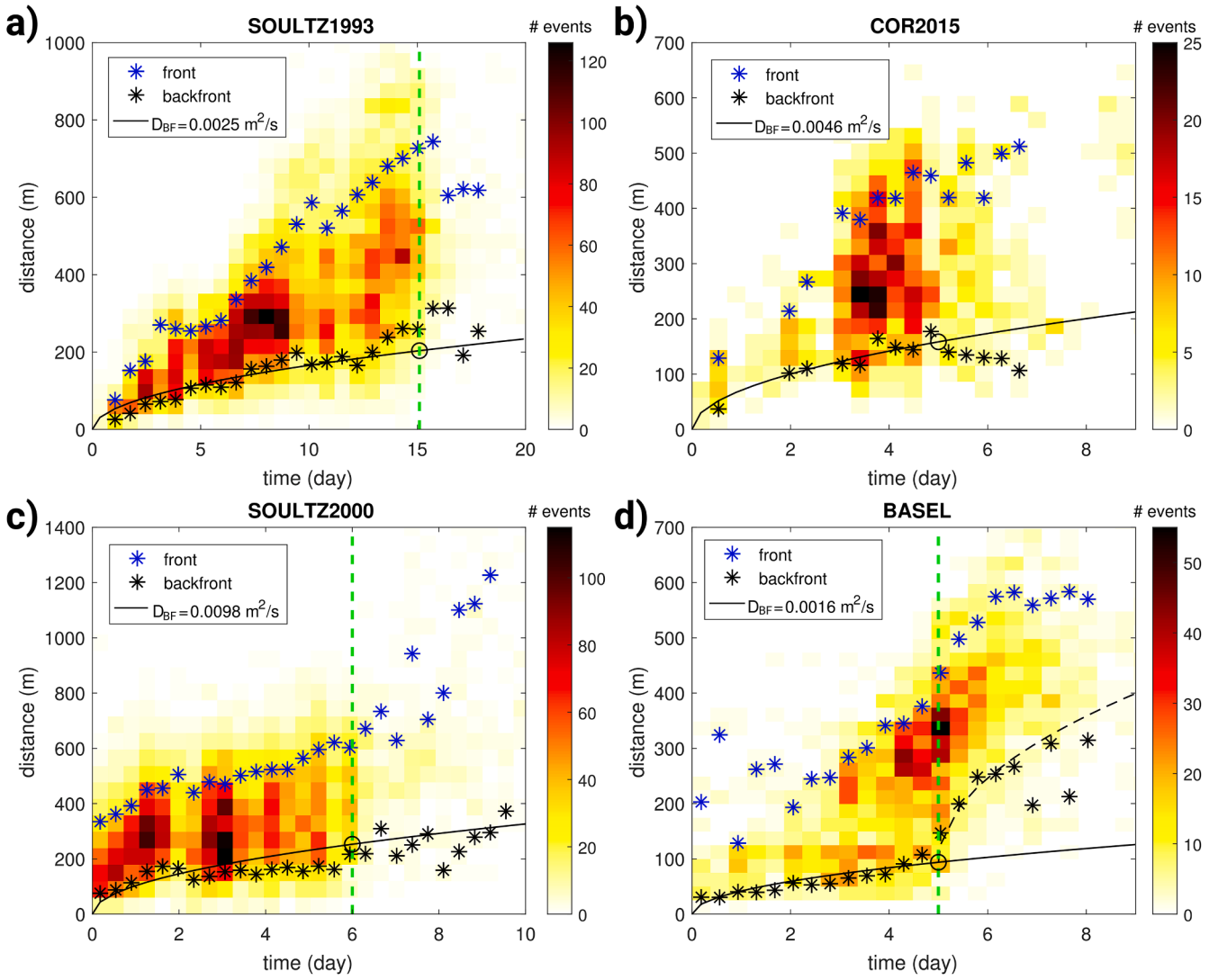

Fig. 1. Density of seismic events depicted in a distance-time plot, where the seismic back-front and front, computed as the 10th and 90th percentile in distance within a sliding time window, are represented by black and blue stars, respectively. The black line shows the diffusive law with apparent diffusivity coefficient D_{BF} that best fits the back-front during the injection period, while the dashed black line in panel (d) represents the post-injection back-front. The green line denotes the injection shut-in time, when known for anthropogenic injections. The black circle indicates the estimated injection end on the fitted diffusive law. (a) and (c) Stimulation for EGS in Soultz-sous-Forêts in 1993 and 2000, respectively; (b) Natural swarm in the Corinth rift in 2015; and, (d) Stimulation for EGS in Basel in 2006. Same figures for other swarms are presented in Supplementary Figs. S2 and S3.

In all swarms, regardless of their natural or anthropogenic origin, a distinct area characterized by either no events or with a very low event density can be observed at small distances from the spatial origin during the injection period (Figs. 1, S2 and S3). Furthermore, this area grows over time, leading to a seismic back-front, similarly to the seismic front. This growing gap during the injection period is also observed when examining the cumulative seismic moment in time-distance plots (Figs. S4 and S5). Additionally, The density of events projected onto the main fault plane directly evidence a growing area with less seismic events close to the injection, as illustrated for the Soultz-sous-Forêts 1993 stimulation shown in Fig. S6. The back-front distances, delineating the distances enclosing 10 % of the events, represent, as a median value over time, between 20 % and up to 60 % (with mean values for all swarms at 35 %) of the front distances, which surround 90 % of the events (Fig. S7). Finally, by considering a lower percentile (2nd instead of 10th one), used to compute the back-front, the latter remains distinctly visible in the distance-time plot (Fig. S8).

The presence of a seismic back-front during the injection phase leads to the observation that there is no specific back-front after the injection shut-in for most sequences. Indeed, the back-front continues to expand, exhibiting a gradual expansion without distinct changes in behavior, after the injection shut-in. In particular, even if this case was widely adopted as reference case for post-injection back-front by many authors (Jacquey and Viesca, 2023; Parotidis et al., 2004; Sáez and Lecampion, 2023), the back-front for the 1993 injection in Soultz-sous-Forêts (Fig. 1a) does not show a specific behavior after the injection shut-in. The apparent post-injection back-front, observed when plotting individual events in the *R-T* domain, is more a visualization artifact arising from the decrease in event rate after the injection shut-in. Only two induced sequences, Basel in 2006 (Fig. 1d) and Cooper Basin in 2003 (Fig. S2) display a clear post-injection back-front, behaving differently from the back-front observed during the injection. Furthermore, none of the natural swarms exhibits a discernible back-front after the end of the migration that could be interpreted as a post-injection back-front.

Traditionally, the seismic front is fitted by a diffusivity law, which links the distance from the injection point (R) to the elapsed injection time (T) as follows (Shapiro et al., 1997):

$$R = \sqrt{4\pi D_F T}, \quad (1)$$

with parameter D_F is a front diffusivity coefficient. This diffusivity coefficient would be categorized "hydraulic" if seismicity was solely induced by the decrease in effective normal stress resulting from the pressure diffusion, However, this assumption does not hold true when the seismic front is driven by fluid-induced aseismic slip (Bhattacharya and Viesca, 2019; De Barros et al., 2021; Eyre et al., 2019). Note that the choice of numerical prefactor π in (1) is `arbitrary' without fault mechanics considerations for the critical value of the induced pore pressure perturbation to trigger seismicity. In line with the seismic front's characteristics and the observed back-front shape (Fig. 1), we applied a diffusivity law to fit it, assuming an apparent diffusivity D_{BF} of the back-front. This coefficient values range from 1×10^{-3} to 1×10^{-1} m^2/s, representing an order of magnitude lower than the diffusivity obtained when fitting the seismic front (Fig. S9). Notably, this range of diffusivity falls below the commonly assumed values for fluid-induced seismicity (Talwani et al., 2007).

The spatial distribution of events across different time intervals (Figs. 2, S10 and S11) consistently validates the emergence of a growing area characterized by limited seismicity close to the injection point. Notably, it reveals a wide peak of seismicity that progressively move away from injection over time. As time elapses, the number of events diminishes near the injection point, indicating the confinement of the seismically slipping region within a wide volume delineated between the seismic front and the back-front.

4. Properties of the vanishing seismicity at the back-front

To understand the origin of the back-front, we delve into the seismic properties. As discussed later in more extensive details, several processes may cause the seismicity to vanish near the injection point. While shear stress dissipation may establish a new equilibrium, potentially resulting in a lack of large events, increased fluid pressure may affect seismic nucleation length, leading to the disappearance of the smallest events. Therefore, we specifically focus on the magnitude evolution of events close to the injection. In this investigation, we establish the minimum magnitude by computing the mean magnitude of the five smallest event, thereby mitigating potential biases introduced by isolated spurious event magnitudes.

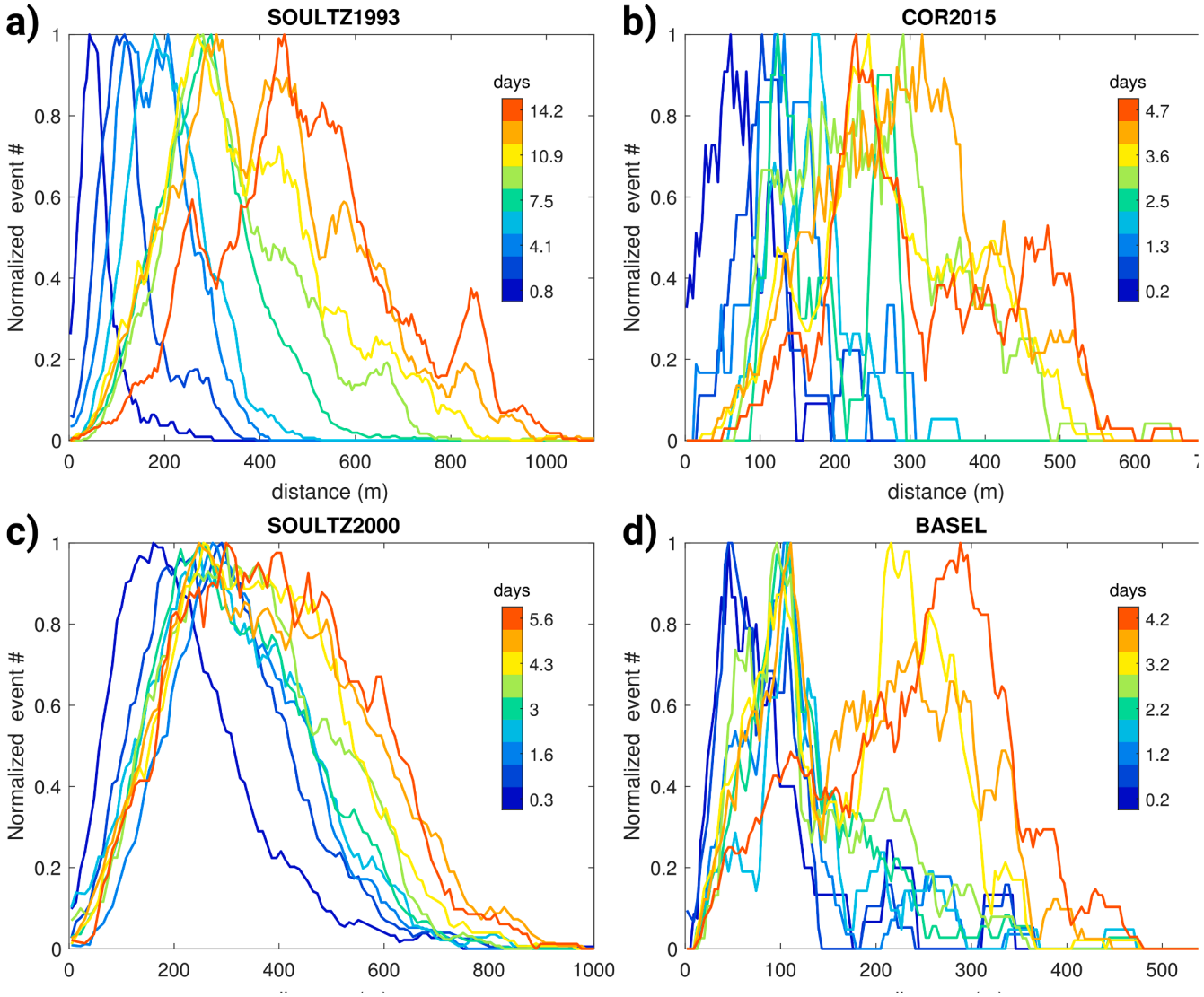

Fig. 2. Normalized spatial distribution of the number of events relative to the distance from the injection across various time windows during the injection period, depicted in a gradient from blue to red. The sequences presented correspond to those in Fig. 1: (a) Soultz-sous-forêts EGS, 1993; (b) Corinth Rift, 2015; (c) Soultz-sous-forêts EGS, 2000; (d) Basel EGS, 2006. The same figures for other sequences can be found in Supplementary Figs. S10 and S11.

4.1. Evolution of magnitude in the time-distance domain

Fig. 3a shows the minimum magnitude on a grid made of 35 cells in distance and time for both the Soultz 1993 EGS and the Cahuilla swarm. Notably, the minimum magnitude is clearly higher at short distances from injection, particularly in the region surrounding the area devoid of seismicity, as compared to the main body of the swarm. The relationship between minimum magnitude with distance (Fig. 3b) cannot be defined at short distances from the spatial origin due to the absence of observed events. Subsequently, it exhibits a sharp decrease with distance before stabilizing at a constant value within the swarm, occasionally displaying an increase at the farthest distance.

Similarly, we examine the temporal evolution of the minimum magnitude within distance ranges where seismicity vanishes. Specifically, we focus on events occurring at distances (R) between 0 and R_{BF}, where R_{BF} corresponds to the distance of the fitted back-front (Eq. (1)) at the shut-in time T_{end} ($R_{BF} = \sqrt{4\ \pi\ D_{BF}\ T_{end}}$, see black circle in Fig. 1). To capture variations over time, we compute the minimum magnitude within this distance range using sliding time windows, each spanning 10 % of the shut-in time. Given the heterogeneity in magnitude measurements across catalogs of the considered sequences, our analysis focus on relative magnitude variations. To achieve this, we correct the measured minimum magnitude within the [0, R_{BF}] range by subtracting the minimum magnitude across all distance ranges. For reference, a parallel analysis is conducted for a distance range between R_{BF} and $2R_{BF}$ within the body of the swarm. Across all 22 swarms under consideration, the corrected minimum magnitude clearly increases over time (Fig. 4a). This observation aligns with the increasing proportion of events occurring behind the back-front as time progresses, confirming that the minimum magnitude is notably elevated close to the back-front. The magnitude increase varies across swarms, ranging up to $\Delta M = 0.8$ for certain sequences, with a median value increase approaching $\Delta M = 0.25$. Importantly, this magnitude elevation is not evident elsewhere in the swarm, as in the reference case where the corrected minimum magnitude remains relatively constant within distances comprised between R_{BF} and $2R_{BF}$, (Fig. 4b). Consequently, this magnitude variation is unlikely to stem from earthquake detection issues, and appears to be associated with a distinct physical process.

4.2. Magnitude evolution across deciles in the R-T domain

The results presented in Figs. 3 and 4 are based on a spatial and temporal grid, a configuration that may introduce bias due to variations in the number of events when computing the minimum magnitude. To validate and refine the observed increase in minimum magnitude at the back-front, we undertake a more nuanced analysis by examining the magnitude evolution within the distance-time domain, categorized into 10 deciles with a similar number of events (Fig. 5a). To achieve this, we

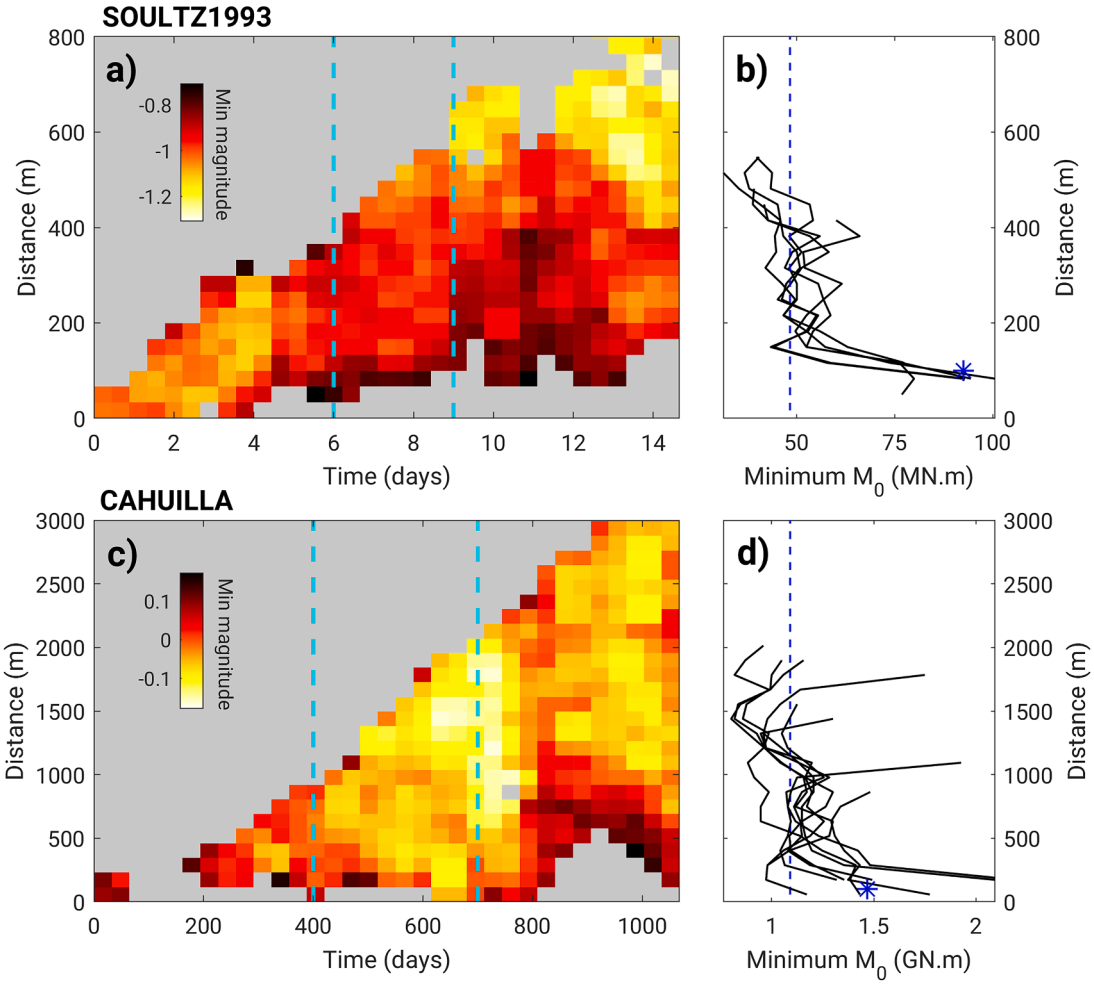

Fig. 3. Minimum magnitude in the distance-time domain during the injection period for (a) Soultz 1993 EGS and (c) the Cahuilla swarm. The minimum magnitude is computed as the average of the five smallest events within 35 windows in time and distance, incorporating a 50 % overlap. Panels (b) and (d) show the equivalent seismic moment versus distance for windows between days 6-to-9, and days 400-to-700, for Soultz 1993 EGS and the Cahuilla swarm (cyan lines in a and b), respectively. The blue dotted line represents the minimum seismic moment, and the star denotes the median maximum value of the minimum seismic moment at short distances.

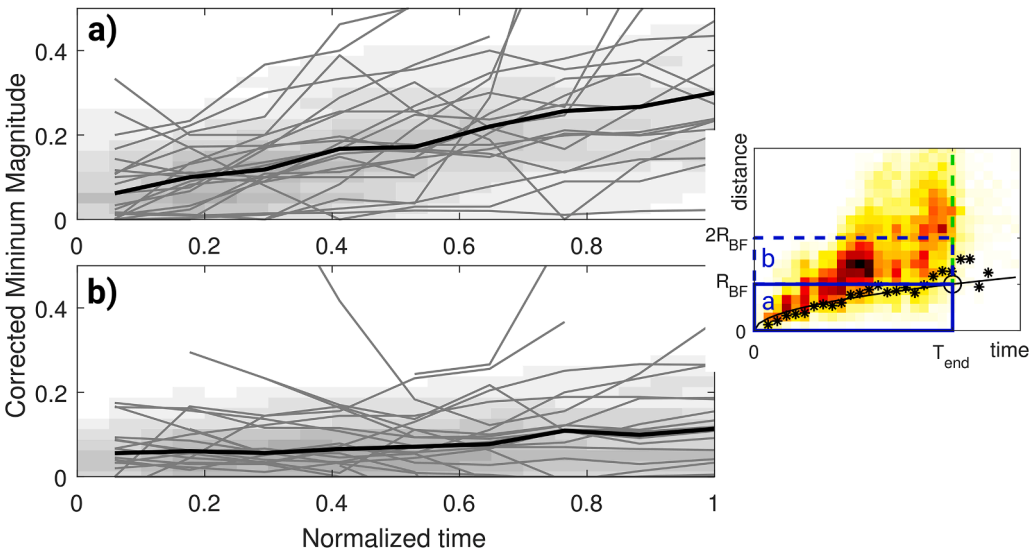

Fig. 4. Minimum magnitude for distances (a) where seismicity disappears close to the injection point ($0 < R < R_{BF}$) and (b) those defined by $R_{BF} < R < 2*R_{BF}$ to act as a reference within the body of the swarm. In both panels, minimum magnitudes, computed in sliding time windows, are corrected by subtracting the minimum magnitude computed for all distances. These values are presented as a function of time normalized by the shut-in time (T/T_{end}). The gray lines depict the magnitude evolution for the 22 swarms, with the gray area indicating the density of measures, and the black line representing the median values.

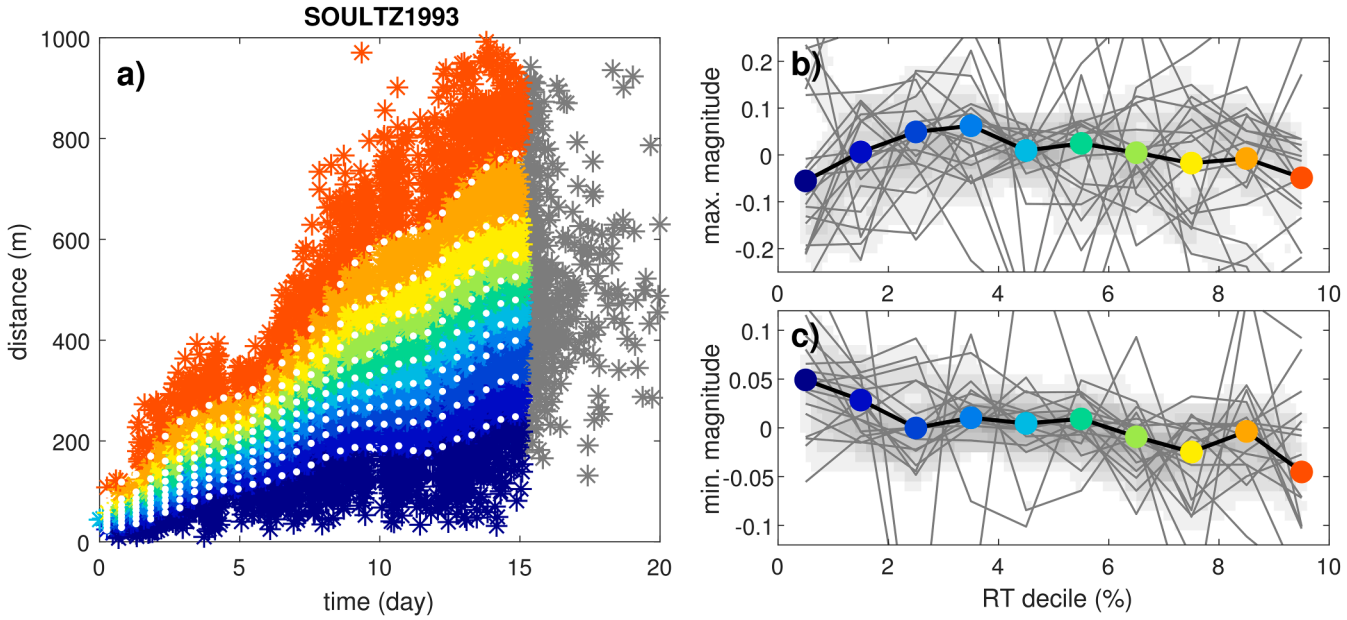

Fig. 5. (a) Example of decile binning in the R-T domain, applied on the Soultz 1993 injection sequence. The white dots show the decile limits, used for categorizing events into 10 distinct color-coded bins. Gray crosses represent events occurring after the shut-in. (b) Maximum and (c) minimum magnitudes versus deciles in the R-T domain for 18 sequences. The maximum and minimum magnitudes are computed as the mean of the five largest and smallest events, respectively, and are corrected by their mean values on the sequence. The gray lines show the measurements for individual sequence, with the gray area indicating the density of measures. The black line represents the median value for all sequences, with dots colored according to the deciles depicted in (a).

determine the event number deciles in a sliding time window, resulting in time curves that are then smoothed using a sliding mean filter applied to three consecutive points. Theses smoothed time curves enable binning the events in the R-T domain in 10 different deciles. It is important to note that due to the smoothing process, there may be slight variation in the number of events between adjacent deciles. Following our definitions of the back-front and the front, the first decile of events is situated behind the back-front, while the 10th is positioned beyond the seismic front.

For each decile, we assess both the maximum and minimum magnitude (Fig. 5b and c). To focus on relative variations among sequences, we correct them by subtracting their mean values. To ensure robust measurements, our analysis is confined to the 18 sequences featuring more than 1000 events, to have at least 100 events per decile. While there may be considerable variations in the minimum and maximum magnitude across sequences, global tendencies can be observed on their median values. The minimum magnitude is high in the first two deciles, remains relatively constant between the 3rd and the 9th

deciles, and experiences a reduction in the 10th decile. Although the relative increase in magnitude in the first decile is small, approximately 0.05, it appears statistically robust. Indeed, we test whether this increase could be an observational artifact by randomly reshuffling the decile positions of the measured minimum magnitudes for each sequence and computing the median minimum magnitude across all sequences. After repeating this process 1000 times, we find that the probability of obtaining a magnitude increase of 0.05 by chance is less than 0.01 % (Supplementary Fig. S12). Thus, reaffirming observations from Figs. 3 and 4, the smallest events appear larger in magnitude close to the back-front compared with the main body of the swarms. Conversely, the maximum magnitude, on average, tends to be smaller near the back-front, while remaining nearly constant or slightly decreasing with increasing decile in the remainder of the R-T domain.

5. Discussion

Examining the distance-time distribution of 22 seismic sequences, arising from either human-induced activity in deep geological reservoirs or natural origins, a consistent observation emerges: a seismic back-front is always present during the swarm's growth phase, aligning with the period of injected fluid pressure. Consequently, seismicity appears confined to a domain delineated between the back-front and the seismic front. This shared behavior across both induced and natural sequences affirms the presence of analogous driving processes in these different settings, as previously demonstrated by Danré et al. (2022).

5.1. Back-front caused by the nucleation length increase with pressure

Observations in geo-energy reservoirs and field experiments at decametric scales consistently reveal a pronounced aseismic component of deformation, particularly close to the injection point (Bourouis and Bernard, 2007; Cornet, 2016; De Barros et al., 2023; Duboeuf et al., 2017; Eyre et al., 2019; Guglielmi et al., 2015b). Consequently, it is highly probable than the absence of seismicity behind the back-front does not signify a lack of slip; rather, it implies a complete transition to aseismic slip.

The Kaiser effect was commonly invoked to explain the post-injection back-front of the seismicity (Shapiro and Dinske, 2007). It corresponds to the fact that seismicity is minimal or absent until surpassing the previous stress or pressure level. In particular, it may apply during multistage injection scenarios (Zang et al., 2014). However, our observations indicate that the back-front occurs at any time, including in phases where the pressure is still increasing at the injection (see examples for the Soultz-sous-Forêts 1993, and Cooper Basin, 2012, Supplementary Fig. S13). Another potential explanation might be linked to the opening of faults. Close to the injection, the high-pressure level may induce tensile failures, resulting in a reduction of contact between fault walls, leading to aseismic deformation close to the injection point. However, the Soultz-sous-Forêts EGS exhibits exclusively shearing events without non-double-couple components (Fischer and Guest, 2011). Moreover, and as discussed later, fault opening is localized near the well (Cornet, 2016) and cannot explain alone the observed paucity of seismicity on much larger scale (~100 m). Injection of cold water in a hot reservoir may also induce thermal stressing of the fault, leading to an aseismic area around the injection point, as the cooling front migrates (Wassing et al., 2021). However, we also observe a back front for natural swarms for which thermal effects are not expected. An alternative mechanism involves fluid pressure stabilizing fault slip, thereby promoting aseismic slip (Cappa et al., 2019). Fault materials exhibiting a rate-weakening behavior may undergo aseismic slip under high fluid pressure. This is primarily attributed to the fact that earthquake nucleation length (L_c), representing the minimum size of a frictionally-weakening fault patch that can nucleate an earthquake instability, predominantly increases with fluid pressure, or equivalently with decreasing effective normal stress. Earthquake rupture mechanics allows estimating L_c as follows (Rice, 1993):

$$L_c = A\,\frac{G\,d_c}{\sigma_n - p} \tag{2}$$

where G is the rock shear modulus, A is a factor that depends on the friction law, σ_n and p the total normal stress and fluid pressure, respectively. Slipping patches with radii greater than the critical nucleation length ($L>L_c$) are susceptible to seismic slip, whereas those with radii $L < L_c$ are not. Assuming a constant shear modulus and a constant seismic stress drop, the magnitude of seismic events varies with the nucleation length, as $M_0 \propto L_c^3$ (Ohnaka, 2000). We here observed (Figs. 3–5) that the minimum magnitude, and consequently, the nucleation length, increases close to the back-front. Considering that the variations in parameters A, G and d_c among seismic asperities and with fluid pressure are of second-order, we assume them constant. We can thus directly relate the increase of minimum magnitudes to an increase in pressure, without resorting to a specific friction law. Therefore, high-fluid pressure in the faults around the injection may result in a purely aseismic slip, as the enlarged nucleation length surpasses the sizes of the asperities. Owing to the process of fluid diffusion, the maximum pressure is observed at the injection point and gradually decays from there as it spreads outward. Consequently, the back-front may correspond to the maximum distance at which the fluid pressure leads to nucleation lengths that are too large to generate seismicity, relative to the sizes of the asperities.

5.2. Theoretical reconstruction of the back-front

This increase of the minimum magnitude, attributed to the expanding nucleation length, can be theoretically reproduced (Fig. 6) assuming fluid pressure diffusion and an elasto-frictional framework suggesting an inverse relation between nucleation length and effective stress. The details of the analysis, applied to the Soultz-sous-Forêts, 1993, EGS stimulation, are given in Appendix. The variation of the minimum seismic moment with distance, at time between 6 and 9 days (Fig. 3b), is first inverted to reconstruct the hydraulic diffusivity and the fluid overpressure-to-stress ratio value. The hydraulic diffusivity D, used in $R = \sqrt{4DT}$ (see appendix), is found to be $D = 0.008$ m^2/s. It is within a factor of π from the diffusivity D_{BF} (D_{BF}=0.0025 m^2/s) obtained by fitting the back-front (Fig. 1 and Eq. (1)). Therefore, it confirms that the back-front is a fluid-pressure front, and suggests that the amended form $R = \sqrt{4DT}$ should be used when fitting the back-front to reconstruct the hydraulic diffusivity D. For the other sequences, the apparent diffusivity coefficients D_{BF} lead to hydraulic diffusivities D falling within the range 1×10^{-3} to 3×10^{-1} m^2/s, with a geometric mean of 2.5×10^{-2} m^2/s. This range of diffusivity better aligns with direct measures of fault diffusivity (Doan et al., 2006; Wibberley, 2002) than the diffusivity range classically considered in interpretation of induced seismicity runouts ($D_F = 0.1$ to 10 m^2/s; Talwani et al., 2007). As measured at the back of the propagating rupture, these values correspond to the diffusivity of faults that were already reactivated, whether seismically or aseismically, resulting in an enhanced permeability (Cappa et al., 2022; Yildirim et al., 2020). Consequently, the inferred diffusivity may represent the hydraulic diffusivity of a highly transmissive medium after permeability enhancement, and serve as an upper bound for the hydraulic diffusivity of the medium before injection.

In our theoretical reconstruction of the 1993 Soultz-sous-Forêts stimulation, the overpressure close to the injection is found to be larger than the normal stress (Fig. 6a), the fault is predicted to open in an area close to the injection. This hydro-fracturing area is however 10 times

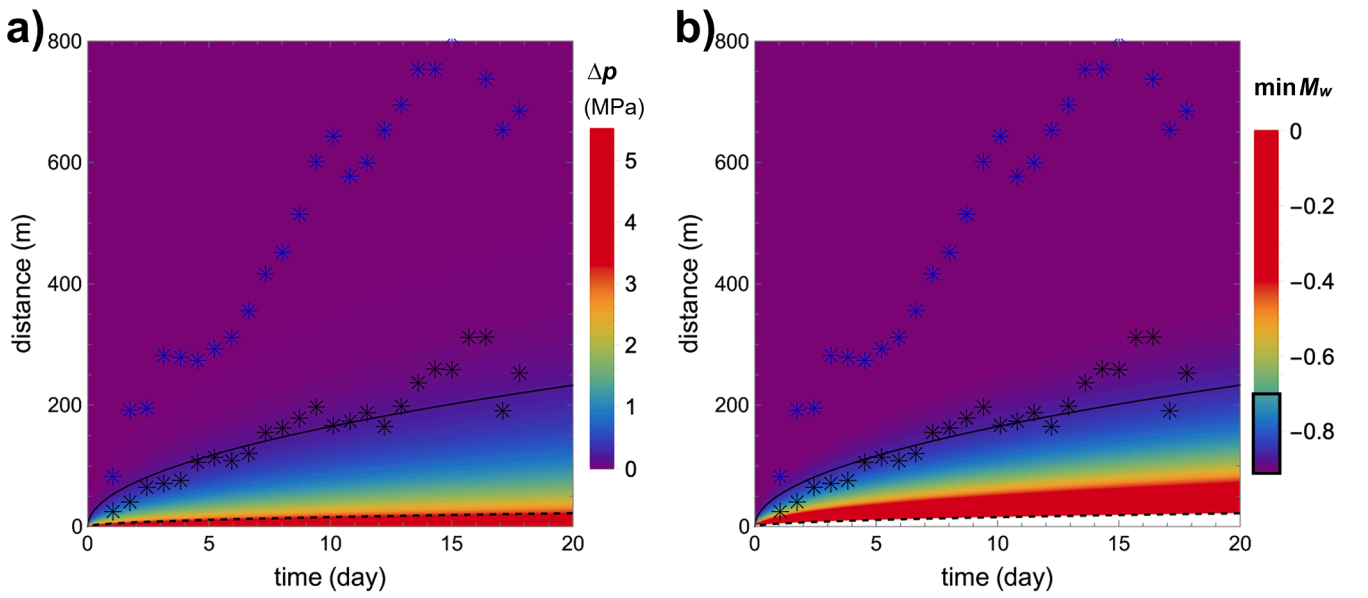

Fig. 6. (a) Fluid overpressure (MPa) computed with the inferred hydraulic diffusivity $D = 0.008$ m^2/s obtained from fitting minimum magnitude – distance relation (Fig. A1) and characteristic value $\Delta p_* = 10$ MPa informed by the maximum treatment wellhead pressure and (b) corresponding theoretical minimum magnitude in distance time domain with the observed range, $-0.9 \leq M_w \leq -0.7$, boxed on the color bar. In both panels, the observed seismic back-front and front are shown by black and blue stars, respectively, while the black line shows the diffusive law fit to the back-front (Fig. 1a). The dotted line is the hydro-fracturing front that delimits the area where tensile failures are expected, hence where magnitude computation diverges. The details of computation are given in Appendix.

smaller than the back-front. Consequently, fault opening alone cannot elucidate the zone devoid of seismicity near the injection. Moreover, although hydro-fracturing is probable in Soultz-sous-Forêts (Cornet, 2016), it is not a prevalent feature in EGS stimulation, as, for example, fluid pressure remains below the minimum stress threshold in Cooper Basin stimulation (Holl and Barton, 2015).

The seismicity develops between the back-front and the seismic front, in an area where fluid overpressure is close to 0 (Fig. 6a). We reconstruct the minimum magnitude evolution in this area (Fig. 6b) to compare it with the observations in Fig. 3. To accomplish this, we first determine the nucleation length at the ambient stress level from the minimum magnitude away from the injection, and then extrapolate its evolution with pressure using Eq. (2) (see Appendix), without relying on any specific friction law. The minimum magnitude is found to increase by nearly 1 when getting close to hydro-fracturing area, compared to the reference minimum magnitude between the back-front and the front. Therefore, the simple theoretical framework shown in Appendix is able to reproduce the observations on the minimum magnitude behaviors (Fig. 3), making it a suitable interpretation for the back-front. It confirms that the vanishing of the seismicity close to the back-front can be explained by the increase of the earthquake nucleation length close to the injection. Moreover, the variations of the minimum magnitude may be used quantitatively to infer the fluid diffusivity and overpressure. However, caution is warranted in this quantitative analysis as the used minimum magnitudes are inherently below the completeness magnitude of the catalogs. Indeed, as low-magnitudes events are missing from the catalogs due to the increase in earthquake nucleation length, the magnitude of completeness must be larger than the reference minimum magnitude. Therefore, the full catalog, including magnitudes below the completeness magnitude, must be considered. Because of possible sampling bias in the magnitude catalog, the observation and the modeling of the back-front are only evidenced from the relative variations of the minimum magnitude, and not on its value itself.

5.3. Generic behaviors of swarms

The systematic observations of a back-front during injection is notable across all natural and injection-induced seismic sequences. In contrast, the occurrence of a post-injection back-front does not appear to be a common feature; it is distinctly observed in only two geothermal stimulations with an abrupt acceleration of the back-front at the shut-in (Basel, 2006 and Cooper Basin, 2012, see Figs. 1 and S2). Particularly, the injection borehole in Basel EGS was opened at the termination, resulting in a fast pressure drop from the injection pressure to hydrostatic levels (Fig. S13, Deichmann and Giardini, 2009). Moreover, flowback at the end of the injection may have also accelerated the back-front, leading to a clear post-injection back-front and a sharp decay in the seismicity rate (Schultz et al., 2023a). On the contrary, boreholes were usually shut down after injection cessation, leading pressure to diffuse and reach equilibrium within the stimulated medium without any abrupt pressure drop. This suggests that the sudden pressure drop may be responsible for the post-injection back-front, generating a locking front propagating from the injection (Jacquey and Viesca, 2023; Sáez and Lecampion, 2023). For natural swarms, fluid pressure likely originates from fault-valve behaviors (Baques et al., 2023; Shelly et al., 2015; Sibson, 1992). The pressurized fluid becomes trapped beneath a caprock, leading to the failures of low-permeability asperities. Subsequently, the fluid diffuses and induces the swarm, following a similar process to that of the anthropogenic injection sequences. When injection stops, either due to pressure equilibrium between the reservoir and the swarm area or the closure of conductive paths within the low permeability asperities, the fluid pressure slowly equilibrates with the surrounding pressure condition without significant drop. In such cases, a post-injection back-front, as observed in Basel EGS, is unlikely for natural swarms, and has not been identified in any of the studied sequences. A back-front in natural swarms (Liu et al., 2023; Mesimeri et al., 2019; Parotidis et al., 2005; Ross and Cochran, 2021) might be therefore more related to the injection period and/or complexities in the fault

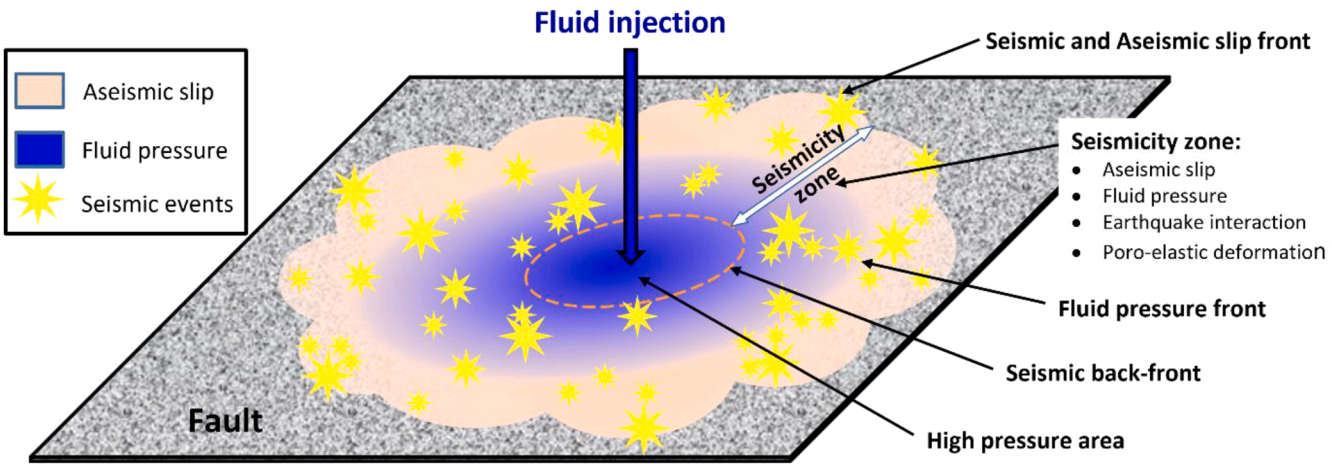

Fig. 7. Conceptual model summarizing the internal process driving the swarm. The seismicity at the front is dominantly driven by fluid-induced aseismic slip, whereas behind the front, fluid pressure assumes a more significant role. It not only triggers a portion of seismicity within the body of the swarms but also prevents seismicity behind the back-front.

structures, rather than serving as a reliable indicator of swarm termination (Parotidis et al., 2005). A refined analysis of migration episodes within the swarms (De Barros et al., 2020) may help to discern if such back-fronts are linked to fault geometries and properties, internal processes or fluid pressure supply.

In summary, our observations reveal a distribution of seismicity extending between the seismic front and the back-front (Fig. 7). Recent models propose that the seismic front is primarily driven by fluid-induced aseismic slip, extending beyond the fluid pressure front (Bhattacharya and Viesca, 2019; Danré et al., 2022; De Barros et al., 2021; Garagash, 2021; Riffault et al., 2018; Sáez and Lecampion, 2023; Wynants-Morel et al., 2020). Within this conceptual framework, seismicity at the front is directly triggered by shear stress concentration at the tips of aseismic slip. Behind the front, seismicity may be triggered by various mechanisms, including aseismic slip (Cappa et al., 2019; De Barros et al., 2019b; Guglielmi et al., 2015a), earthquake interactions and cascading events (Daniel et al., 2011; Dublanchet and De Barros, 2021; Fischer and Hainzl, 2021; Glasgow et al., 2023), poroelastic deformation (Goebel and Brodsky, 2018; Segall and Lu, 2015), or directly by fluid pressure reducing the normal stress on the fault (Shapiro et al., 1997). Numerical modeling supports this, indicating that, for the 2012 Cooper Basin injection, seismicity beyond half of the cloud size is mainly driven by aseismic slip, while direct fluid pressure effects dominate at shorter distances (Wang and Dunham, 2022). Our results demonstrate that seismicity vanishes behind a back-front, a phenomenon we interpret as an increase of the earthquake nucleation length surpassing the sizes of asperities. At even shorter distances from the injection, possible fault opening might also prevent seismicity to occur. Consequently, the seismicity distribution looks like an extended pulse-like rupture. However, the total slip (aseismic and seismic components) follows a crack-like rupture (Danré et al., 2024; Garagash, 2021), with the seismic slip representing a back-truncated version of it.

6. Conclusion

Through the analysis of 22 seismic sequences, we have identified a consistent presence of a seismic back-front, characterized by a progressively expanding area at the center of swarm devoid of seismic events. This behavior is observed on both natural swarms and sequences induced by EGS stimulations, highlighting the similarity of underlying processes in both types of sequences. We have not yet explored if this back-front behavior can be generalized to more complex swarms, including sequences induced by long-lasting injections, dominated by poroelastic deformation, or occurring in highly heterogeneous materials.

Our observations reveal that small magnitude events tend to disappear first within this back-front area. This behavior may be attributed to an increase in earthquake nucleation length resulting from elevated fluid pressure. The theoretical computation of the nucleation length evolution with pressure allows us to reproduce the magnitude observations in 1993 Soultz-sous-Forêts EGS, validating this interpretation. Consequently, such a back-front cannot be used to infer the cessation of injection, as is classically done for natural swarms. Notably, the post-injection back-front appears to be a rare feature occurring only in induced sequences marked by a sharp pressure drop.

This result holds potential for quantitative applications in deducing variations in earthquake nucleation length and pressure. However, it is important to acknowledge that the smallest magnitude events considered in this analysis fall inherently below the magnitude of completeness. To comprehensively explore and quantify the back-front during injection, the development of enhanced catalogs, derived through improved detection using template-matching or deep-learning techniques applied to high-resolution seismological networks, becomes a prerequisite for future investigations.

Data availability

The supplementary table S1 summarizes the source of seismic catalogs used in this study. We thank J. Albaric (Albaric et al., 2014) for providing the Paralana sequence and G. Daniel (Daniel et al., 2011) for the Ubaye swarm catalogs. All other seismic catalogs are publically available in data repositories, with all references needed to access the data in supplementary materials (see table S1).

CRediT authorship contribution statement

Louis De Barros: Writing – original draft, Funding acquisition, Formal analysis, Data curation, Conceptualization. **Philippe Danré:** Writing – review & editing, Formal analysis, Data curation, Conceptualization. **Dmitry Garagash:** Writing – review & editing, Validation, Formal analysis, Conceptualization. **Frédéric Cappa:** Writing – review & editing, Validation, Formal analysis. **Olivier Lengliné:** Writing –

review & editing, Validation, Formal analysis, Data curation.

Declaration of competing interest

The authors declare that they have no known competing financial interests or personal relationships that could have appeared to influence the work reported in this paper.

Data availability

The supplementary table S1 summarizes the source of seismic catalogs used in this study. We thank J. Albaric (Albaric et al., 2014) for providing the Paralana sequence and G. Daniel (Daniel et al., 2011) for the Ubaye swarm catalogs. All other seismic catalogs are publically available in data repositories, with all references needed to access the data in supplementary materials (see table S1).

Acknowledgment

This work was supported by the Agence Nationale de la Recherche (ANR) through the INSeis project under contract ANR-22-CE49-0018. We are grateful to the editor (H. Thybo) and the two reviewers (E. Dunham and R. Schultz) for their helpful comments.

Supplementary materials

Supplementary material associated with this article can be found, in the online version, at doi:10.1016/j.epsl.2024.118849.

Appendix

In this Appendix, we consider modeling the minimum induced earthquake moment magnitude on a fault pressurized by fluid injection. For simplicity, consider fluid injection into a conductive fault rock unit of thickness w at a constant volumetric rate q. Corresponding pore pressure perturbation $\Delta p = p - p_o$ can be modelled by the axisymmetric point-source solution on lengthscales larger than the fault thickness w, (Garagash and Germanovich, 2012; Sáez et al., 2022):

$$\Delta p(r,t) = \Delta p_* \Pi\left(\frac{r}{\sqrt{4Dt}}\right) \tag{A1}$$

where r is the distance from the source along the fault plane, t is the time since the onset of injection, D is the hydraulic diffusivity, $\Delta p_* = q\eta\,/kw$ is the characteristic value of the overpressure expressed in terms of the fluid injection rate per unit fault thickness, q/w, fluid viscosity η, and permeability k, and $\Pi(\xi) = (4\pi)^{-1}\mathrm{E}_1\left(\xi^2\right)$ is the spatio-temporal distribution function expressed in terms of the exponential integral E_1.

Earthquake nucleation patch size, Eq. (2), depends on the local fluid overpressure, and can be expressed in view of Eq. (A1) as

$$L_c(r,t) = \frac{L_{c,o}}{1 - \dfrac{\Delta p(r,t)}{\overline{\sigma}_{n,o}}} \tag{A2}$$

where $L_{c,o} = \frac{A\ G\ d_c}{\overline{\sigma}_{n,o}}$ is the nucleation length at the ambient effective stress $\overline{\sigma}_{n,o} = \sigma_n - p_o$ (Rice, 1993; Segall, 2010).

Corresponding minimum earthquake moment can then be estimated assuming a constant stress-drop rupture of radius L_c

$$M_c(r,t) = M_{c,o}\left[1 - \frac{\Delta p_*}{\overline{\sigma}_{n,o}}\Pi\left(\frac{r}{\sqrt{4Dt}}\right)\right]^{-3} \tag{A3}$$

where $M_{c,o} = \left(\frac{16}{7}\right)\Delta\tau L_{c,o}^3$ is the minimum moment at the ambient conditions and $\Delta\tau$ is the stress drop.

Eq. (A3) predicts a fall-off of the minimum moment with the distance away from the well, consistent with the observations from swarms (Fig. 3). We therefore use Eq. (A3) in a quantitative manner to invert the observations for the underlining diffusion (i.e. diffusivity D and normalized value of the characteristic overpressure $\Delta p_*/\overline{\sigma}_{n,o}$) and the ambient value of the minimum seismic moment $M_{c,o}$. Using the Soultz 1993 sequence data averaged over the time window between from 6 to 9 days (Fig. 3b), i.e. at mean $t = 7.5$ days, we recover from the inversion $M_{c,o} = 49$ MN.m, $D = 0.008$ m^2/s, and $\Delta p_*/\overline{\sigma}_{n,o} = 3$. Fig. A1a shows the best-fit to the minimum seismic moment – distance observations. Fig. A1b shows the fitting (sqrt-mean) error in the space of diffusivity D and the overpressure-stress ratio $\Delta p_*/\overline{\sigma}_{n,o}$ at fixed value of the ambient minimum moment $M_{c,o} = 49$ MN.m. The latter shows the increasing error and the diffusivity value if a smaller vales of overpressure ratio are assumed (i.e., $\Delta p_*/\overline{\sigma}_{n,o} < 3$).

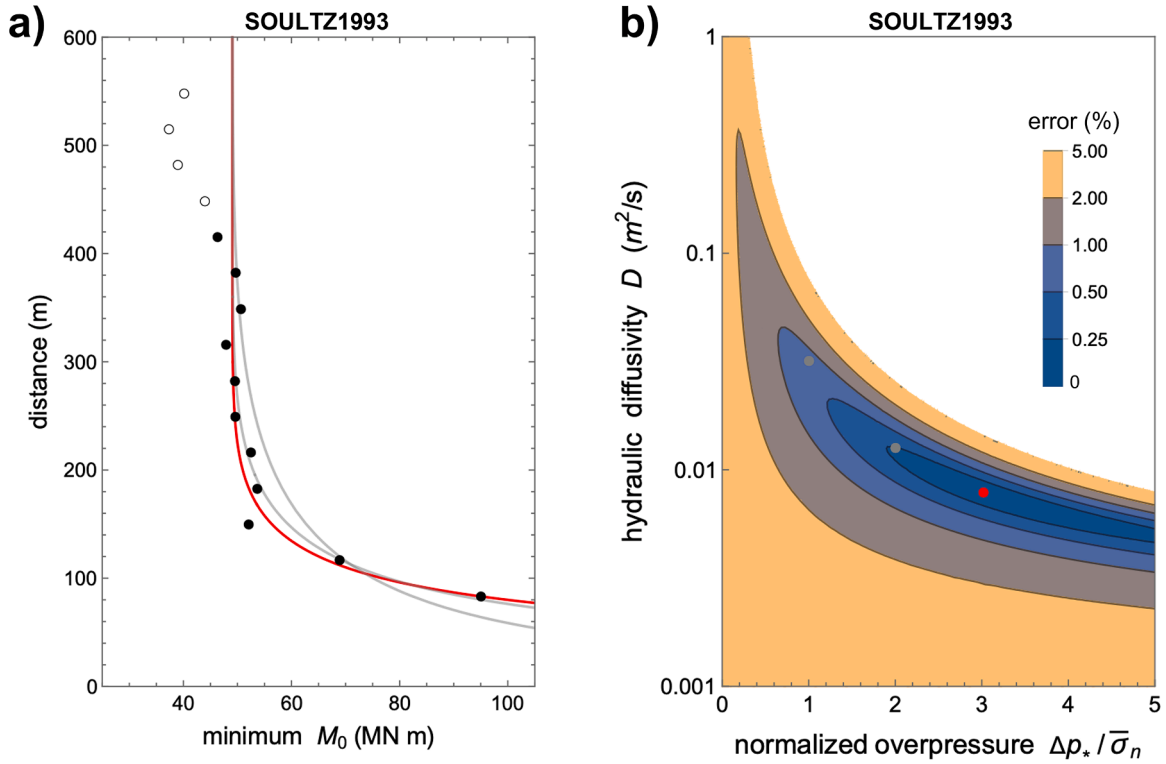

Fig. A1. (a) Minimum seismic moment with distance away from the fluid source in the Soultz 1993 swarm time-averaged from 6-to-9 days (symbols). The black line shows the best fit with Eq. (A3) corresponding to $M_{c,o} = 49$ MN.m, $D = 0.008$ m2/s and $\Delta p_*/\overline{\sigma}_{n,o} = 3$. The gray lines show fits constrained to the same value of $M_{c,o}$ and to a smaller fixed value of the normalized characteristic overpressure $\Delta p_*/\overline{\sigma}_{n,o} = 2$ or 1, respectively, resulting in deteriorating fit and larger hydraulic diffusivity. The far field data, distance > 420 m (open circles), characterized by yet smaller values of the moment are excluded from the fit. (b) Square root-mean error of the fit in the space of characteristic overpressure and diffusivity for the fixed value of $M_{c,o} = 49$ MN m. The best-fit and the two constrained fits (using $\Delta p_* / \overline{\sigma}_{n,o} = 2$ or 1) from (a) are shown by the red and gray symbols, respectively.

Using the reported fluid pressure at the wellhead in Soultz 1993 treatment ≈ 10 MPa (Fig. S13) to inform the characteristic fluid overpressure Δp_* at the injection depth (Eq. (A1)), we infer from the best fit overpressure-to-stress ratio value in our analysis that the ambient effective stress normal to the fault is $\overline{\sigma}_{n,o} \approx 3.3$ MPa. This value is smaller than the $\overline{\sigma}_{min,o} \approx 9$ MPa inferred for the minimum horizontal effective stress at 3 km depth by Valley and Evans (2007), based on the absolute stress estimate ≈ 39 MPa and assuming hydrostatic ambient pore pressure ≈ 30 MPa. We note that assuming a moderate ambient pore fluid overpressure of $\sim$20 % would rectify the difference, i.e. decrease the estimate of $\overline{\sigma}_{min,o}$ to the value of $\overline{\sigma}_{n,o} \approx 3.3$ MPa in our analysis. As far as we know, no direct measurement of the ambient pore pressure at depth at Soultz is available, while generally some level of the ambient pore fluid overpressure, in excess of hydrostatic, can be expected at depth. We also caution that this analysis does not include factors such as thermal and poroelastic effects which could modify the values of inferred pore pressure and stress at depth.

We present the time-distance plot of the treatment overpressure in Fig. A2. Since the injection overpressure exceeds the ambient effective normal stress, the fault is predicted to open in direct vicinity of the fluid source. The extent of this hydro-fracture condition is however is limited to $\sim$ 10 m from the source on the timescale of injection (dashed black line, $R_{HF} \approx 0.09\sqrt{4Dt}$), which is about ten-fold smaller than the inferred domain devoid of seismicity ($\sim$100 m) bounded by the 'seismicity back-front' (solid black line, $R_{BF} \approx \sqrt{4Dt}$). In other words, fault opening localized near the well, as also suggested by Cornet (2016) cannot explain the paucity in seismicity.

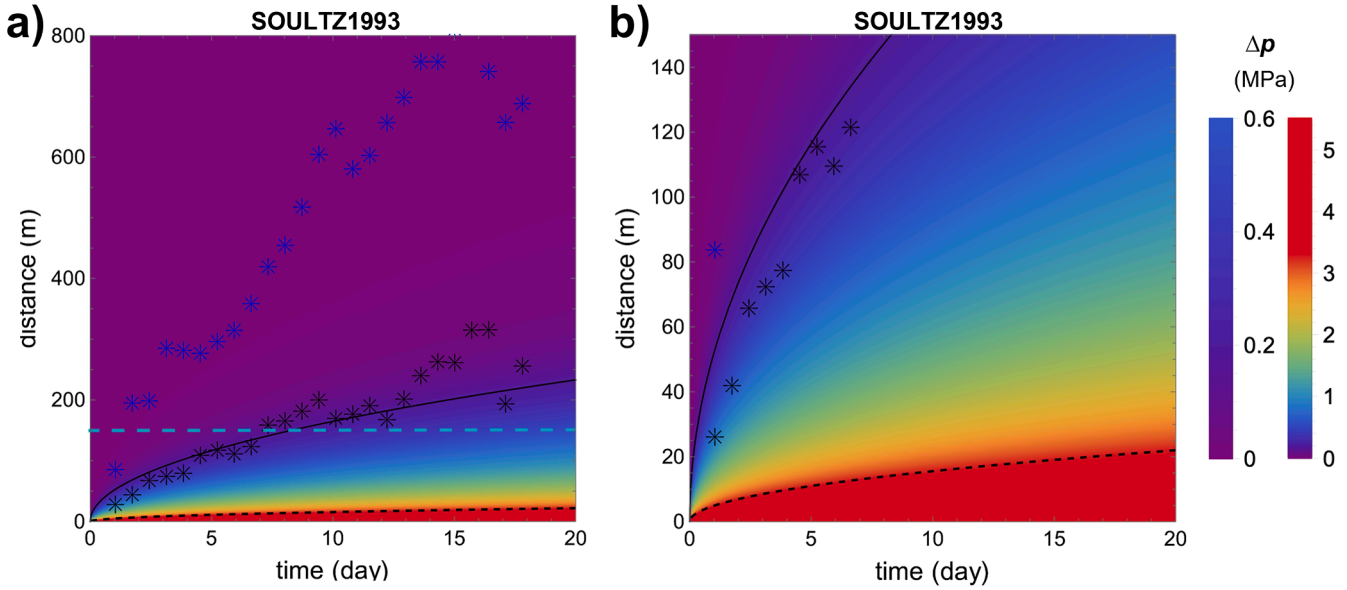

Fig. A2. (a) Fluid overpressure (MPa) in the time-distance domain, (Eq. (A1)) parametrized by hydraulic diffusivity $D = 0.008$ m^2/s obtained from fitting minimum magnitude – distance relation (Fig. A1) and characteristic value $\Delta p_* = 10$ MPa informed by the maximum treatment wellhead pressure. (b) Same as (a) but within 150 m from the fluid source (cyan dashed line in (a)). Black dashed line shows the extent of hydro-fracking (fault opening condition $\Delta p(r,t) \geq \bar{\sigma}_{n,o}$), while the solid line shows the inferred seismicity back-front (Fig. 1a). The open-fault distance is at least an order of magnitude smaller (~ 10 m) and thus localized near the fluid source compared to the seismicity back-front (~100 m) suggesting that the fault opening cannot explain the much larger size of the domain devoid of seismicity.

References

Albaric, J., Oye, V., Langet, N., Hasting, M., Lecomte, I., Iranpour, K., Messeiller, M., Reid, P., 2014. Monitoring of induced seismicity during the first geothermal reservoir stimulation at Paralana, Australia. Geothermics 52, 120–131.

Baisch, S., Rothert, E., Stang, H., Vörös, R., Koch, C., McMahon, A., 2015. Continued geothermal reservoir stimulation experiments in the cooper basin (Australia). Bull. Seismol. Soc. Am. 105, 198–209. https://doi.org/10.1785/0120140208.

Baisch, S., Weidler, R., Voros, R., Wyborn, D., de Graaf, L., 2006. Induced Seismicity during the Stimulation of a Geothermal HFR Reservoir in the Cooper Basin, Australia. Bull. Seismol. Soc. Am. 96, 2242–2256. https://doi.org/10.1785/0120050255.

Baques, M., De Barros, L., Godano, M., Duverger, C., Jomard, H., 2023. Swarms and mainshock–aftershocks sequences are both triggered by fluids in the Ubaye Region (Western Alps). Geophys. J. Int. 235, 920–941. https://doi.org/10.1093/gji/ggad280.

Bhattacharya, P., Viesca, R.C., 2019. Fluid-induced aseismic fault slip outpaces pore-fluid migration. Science 364, 464–468. https://doi.org/10.1126/science.aaw7354.

Bourouis, S., Bernard, P., 2007. Evidence for coupled seismic and aseismic fault slip during water injection in the geothermal site of Soultz (France), and implications for seismogenic transients. Geophys. J. Int. 169, 723–732.

Cappa, F., Guglielmi, Y., De Barros, L., 2022. Transient evolution of permeability and friction in a slowly slipping fault activated by fluid pressurization. Nat. Commun. 13, 3039. https://doi.org/10.1038/s41467-022-30798-3.

Cappa, F., Scuderi, M.M., Collettini, C., Guglielmi, Y., Avouac, J.P., 2019. Stabilization of fault slip by fluid injection in the laboratory and *in situ*. Sci. Adv. 5, eaau4065. https://doi.org/10.1126/sciadv.aau4065.

Cauchie, L., Lengliné, O., Schmittbuhl, J., 2020. Seismic asperity size evolution during fluid injection: case study of the 1993 Soultz-sous-Forêts injection. Geophys. J. Int. 221, 968–980.

Cornet, F.H., 2016. Seismic and aseismic motions generated by fluid injections. Geomech. Energy Environ. 5, 42–54. https://doi.org/10.1016/j.gete.2015.12.003.

Cuenot, N., Dorbath, C., Dorbath, L., 2008. Analysis of the microseismicity induced by fluid injections at the EGS site of Soultz-sous-Forêts (Alsace, France): implications for the characterization of the geothermal reservoir properties. Pure Appl. Geophys. 165, 797–828. https://doi.org/10.1007/s00024-008-0335-7.

Dahm, T., Hainzl, S., Fischer, T., 2010. Bidirectional and unidirectional fracture growth during hydrofracturing: role of driving stress gradients. J. Geophys. Res. Solid Earth 115. https://doi.org/10.1029/2009JB006817.

Daniel, G., Prono, E., Renard, F., Thouvenot, F., Hainzl, S., Marsan, D., Helmstetter, A., Traversa, P., Got, J.L., Jenatton, L., 2011. Changes in effective stress during the 2003–2004 Ubaye seismic swarm, France. J. Geophys. Res. Solid Earth 116, B01309.

Danré, P., De Barros, L., Cappa, F., Ampuero, J.P., 2022. Prevalence of aseismic slip linking fluid injection to natural and anthropogenic seismic swarms. J. Geophys. Res. Solid Earth, 127 (12), e2022JB025571.

Danré, P., De Barros, L., Cappa, F., 2023. Inferring fluid volume during earthquake swarms using seismic catalogues. Geophys. J. Int. 232, 829–841. https://doi.org/10.1093/gji/ggac345.

Danré, P., Garagash, D., De Barros, L., Cappa, F., Ampuero, J.P., 2024. Control of seismicity migration in earthquake swarms by injected fluid volume and aseismic crack propagation. J. Geophys. Res. Solid Earth, 129 (1), e2023JB027276.

De Barros, L., Baques, M., Godano, M., Helmstetter, A., Deschamps, A., Larroque, C., Courboulex, F., 2019a. Fluid-induced swarms and coseismic stress transfer: a dual process highlighted in the aftershock sequence of the 7 April 2014 Earthquake (Ml 4.8, Ubaye, France). J. Geophys. Res. Solid Earth 124, 3918–3932. https://doi.org/10.1029/2018JB017226.

De Barros, L., Cappa, F., Deschamps, A., Dublanchet, P., 2020. Imbricated aseismic slip and fluid diffusion drive a seismic swarm in the Corinth gulf, Greece. Geophys. Res. Lett. 47, e2020GL087142 https://doi.org/10.1029/2020GL087142.

De Barros, L., Cappa, F., Guglielmi, Y., Duboeuf, L., Grasso, J.R., 2019b. Energy of injection-induced seismicity predicted from *in-situ* experiments. Sci. Rep. 9, 4999. https://doi.org/10.1038/s41598-019-41306-x.

De Barros, L., Guglielmi, Y., Cappa, F., Nussbaum, C., Birkholzer, J., 2023. Induced microseismicity and tremor signatures illuminate different slip behaviours in a natural shale fault reactivated by a fluid pressure stimulation (Mont Terri). Geophys. J. Int. 235 (1), 531–541.

De Barros, L., Guglielmi, Y., Rivet, D., Cappa, F., Duboeuf, L., 2018. Seismicity and fault aseismic deformation caused by fluid injection in decametric *in-situ* experiments. C. R. Geosci. 350, 464–475. https://doi.org/10.1016/j.crte.2018.08.002.

De Barros, L., Wynants-Morel, N., Cappa, F., Danré, P., 2021. Migration of fluid-induced seismicity reveals the seismogenic state of faults. J. Geophys. Res. Solid Earth 126, e2021JB022767. https://doi.org/10.1029/2021JB022767.

Deichmann, N., Giardini, D., 2009. Earthquakes induced by the stimulation of an enhanced geothermal system below Basel (Switzerland). Seismol. Res. Lett. 80, 784–798.

Doan, M.L., Brodsky, E.E., Kano, Y., Ma, K.F., 2006. *In situ* measurement of the hydraulic diffusivity of the active Chelungpu Fault, Taiwan. Geophys. Res. Lett. 33 https://doi.org/10.1029/2006GL026889.

Drif, K., Lengliné, O., Kinscher, J., Schmitbuhl, J., 2024. Induced seismicity controlled by injected hydraulic energy: the case study of the EGS Soultz-Sous-Forêts Site. J. Geophys. Res. Solid Earth 129 (6), e2023JB028190.

Dublanchet, P., De Barros, L., 2021. Dual seismic migration velocities in seismic swarms. Geophys. Res. Lett. 48, e2020GL090025 https://doi.org/10.1029/2020GL090025.

Duboeuf, L., De Barros, L., Cappa, F., Guglielmi, Y., Deschamps, A., Seguy, S., 2017. Aseismic motions drive a sparse seismicity during fluid injections into a fractured zone in a carbonate reservoir. J. Geophys. Res. Solid Earth 122, 8285–8304.

Ellsworth, W.L., 2013. Injection-induced earthquakes. Science 341, 1225942.

Eyre, T.S., Eaton, D.W., Garagash, D.I., Zecevic, M., Venieri, M., Weir, R., Lawton, D.C., 2019. The role of aseismic slip in hydraulic fracturing–induced seismicity. Sci. Adv. 5, eaav7172. https://doi.org/10.1126/sciadv.aav7172.

Fischer, T., Guest, A., 2011. Shear and tensile earthquakes caused by fluid injection. Geophys. Res. Lett. 38 https://doi.org/10.1029/2010GL045447.

Fischer, T., Hainzl, S., 2021. The growth of earthquake clusters. Front. Earth Sci. 9 https://doi.org/10.3389/feart.2021.638336.

Fischer, T., Horálek, J., Hrubcová, P., Vavryčuk, V., Bräuer, K., Kämpf, H., 2014. Intra-continental earthquake swarms in West-Bohemia and Vogtland: a review. Tectonophysics 611, 1–27. https://doi.org/10.1016/j.tecto.2013.11.001.

Foulger, G.R., Wilson, M.P., Gluyas, J.G., Julian, B.R., Davies, R.J., 2018. Global review of human-induced earthquakes. Earth Sci. Rev. 178, 438–514. https://doi.org/10.1016/j.earscirev.2017.07.008.

Garagash, D.I., 2021. Fracture mechanics of rate-and-state faults and fluid injection induced slip. Philos. Trans. R. Soc. A 379, 20200129. https://doi.org/10.1098/rsta.2020.0129.

Garagash, D.I., Germanovich, L.N., 2012. Nucleation and arrest of dynamic slip on a pressurized fault. J. Geophys. Res. Solid Earth 117, B10310. https://doi.org/10.1029/2012JB009209.

Glasgow, M.E., Schmandt, B., Bilek, S.L., 2023. Cascading multi-segment rupture in an injection-induced earthquake sequence with a Mw 5.3 mainshock. Earth Planet. Sci. Lett. 620, 118335 https://doi.org/10.1016/j.epsl.2023.118335.

Goebel, T.H.W., Brodsky, E.E., 2018. The spatial footprint of injection wells in a global compilation of induced earthquake sequences. Science 361, 899–904. https://doi.org/10.1126/science.aat5449.

Grigoli, F., Cesca, S., Rinaldi, A.P., Manconi, A., López-Comino, J.A., Clinton, J.F., Westaway, R., Cauzzi, C., Dahm, T., Wiemer, S., 2018. The November 2017 Mw 5.5 Pohang earthquake: a possible case of induced seismicity in South Korea. Science 360, 1003–1006. https://doi.org/10.1126/science.aat2010.

Guglielmi, Y., Cappa, F., Avouac, J.P., Henry, P., Elsworth, D., 2015a. Seismicity triggered by fluid injection–induced aseismic slip. Science 348, 1224–1226. https://doi.org/10.1126/science.aab0476.

Guglielmi, Y., Elsworth, D., Cappa, F., Henry, P., Gout, C., Dick, P., Durand, J., 2015b. *In situ* observations on the coupling between hydraulic diffusivity and displacements during fault reactivation in shales. J. Geophys. Res. Solid Earth 120, 7729–7748. https://doi.org/10.1002/2015JB012158.

Herrmann, M., Kraft, T., Tormann, T., Scarabello, L., Wiemer, S., 2019. A consistent high-resolution catalog of induced seismicity in basel based on matched filter detection and tailored post-processing. J. Geophys. Res. Solid Earth 124, 8449–8477. https://doi.org/10.1029/2019JB017468.

Holl, H.G., Barton, C., 2015. Habanero field-structure and state of stress. In: Proceedings of the World Geothermal Congress, pp. 19–25.

Jacquey, A.B., Viesca, R.C., 2023. Nucleation and arrest of fluid-induced aseismic slip. Geophys. Res. Lett. 50, e2022GL101228 https://doi.org/10.1029/2022GL101228.

Jenatton, L., Guiguet, R., Thouvenot, F., Daix, N., 2007. The 16,000-event 2003–2004 earthquake swarm in Ubaye (French Alps). J. Geophys. Res. Solid Earth 112, B11304. https://doi.org/10.1029/2006JB004878.

Keranen, K.M., Weingarten, M., 2018. Induced seismicity. Annu. Rev. Earth Planet. Sci. 46, 149–174. https://doi.org/10.1146/annurev-earth-082517-010054.

Kwiatek, G., Saarno, T., Ader, T., Bluemle, F., Bohnhoff, M., Chendorain, M., Dresen, G., Heikkinen, P., Kukkonen, I., Leary, P., Leonhardt, M., Malin, P., Martínez-Garzón, P., Passmore, K., Passmore, P., Valenzuela, S., Wollin, C., 2019. Controlling fluid-induced seismicity during a 6.1-km-deep geothermal stimulation in Finland. Sci. Adv. 5, eaav7224. https://doi.org/10.1126/sciadv.aav7224.

Lengliné, O., Boubacar, M., Schmittbuhl, J., 2017. Seismicity related to the hydraulic stimulation of GRT1, Rittershoffen, France. Geophys. J. Int. 208, 1704–1715.

Liu, M., Li, L., Zhang, M., Lei, X., Nedimović, M.R., Plourde, A.P., Guo, R., Wang, W., Li, H., 2023. Complexity of initiation and evolution of the 2013 Yunlong earthquake swarm. Earth Planet. Sci. Lett. 612, 118168 https://doi.org/10.1016/j.epsl.2023.118168.

Martínez-Garzón, P., Kwiatek, G., Sone, H., Bohnhoff, M., Dresen, G., Hartline, C., 2014. Spatiotemporal changes, faulting regimes, and source parameters of induced seismicity: a case study from The Geysers geothermal field. J. Geophys. Res. Solid Earth 119, 8378–8396. https://doi.org/10.1002/2014JB011385.

Mesimeri, M., Karakostas, V., Papadimitriou, E., Tsaklidis, G., 2019. Characteristics of earthquake clusters: application to western Corinth Gulf (Greece). Tectonophysics 767, 228160. https://doi.org/10.1016/j.tecto.2019.228160.

Ohnaka, M., 2000. A physical scaling relation between the size of an earthquake and its nucleation zone size. Pure Appl. Geophys. 157, 2259–2282. https://doi.org/10.1007/PL00001084.

Pacchiani, F., Lyon-Caen, H., 2010. Geometry and spatio-temporal evolution of the 2001 Agios Ioanis earthquake swarm (Corinth Rift, Greece). Geophys. J. Int. 180, 59–72.

Parotidis, M., Shapiro, S.A., Rothert, E., 2005. Evidence for triggering of the Vogtland swarms 2000 by pore pressure diffusion. J. Geophys. Res. Solid Earth 110. https://doi.org/10.1029/2004JB003267.

Parotidis, M., Shapiro, S.A., Rothert, E., 2004. Back front of seismicity induced after termination of borehole fluid injection. Geophys. Res. Lett. 31, L02612. https://doi.org/10.1029/2003GL018987.

Passarelli, L., Heryandoko, N., Cesca, S., Rivalta, E., Rasmid, Rohadi, S., Dahm, T., Milkereit, C., 2018. Magmatic or not magmatic? The 2015–2016 seismic swarm at the long-Dormant Jailolo Volcano, West Halmahera, Indonesia. Front. Earth Sci. 6 https://doi.org/10.3389/feart.2018.00079.

Rice, J.R., 1993. Spatio-temporal complexity of slip on a fault. J. Geophys. Res. Solid Earth 98, 9885–9907. https://doi.org/10.1029/93JB00191.

Riffault, J., Dempsey, D., Karra, S., Archer, R., 2018. Microseismicity cloud can be substantially larger than the associated stimulated fracture volume: the case of the paralana enhanced geothermal system. J. Geophys. Res. Solid Earth 123, 6845–6870. https://doi.org/10.1029/2017JB015299.

Ross, Z.E., Cochran, E.S., 2021. Evidence for latent crustal fluid injection transients in Southern California from long-duration earthquake swarms. Geophys. Res. Lett. 48, e2021GL092465 https://doi.org/10.1029/2021GL092465.

Ross, Z.E., Cochran, E.S., Trugman, D.T., Smith, J.D., 2020. 3D fault architecture controls the dynamism of earthquake swarms. Science 368, 1357–1361.

Ruhl, C.J., Abercrombie, R.E., Smith, K.D., Zaliapin, I., 2016. Complex spatiotemporal evolution of the 2008 Mw 4.9 Mogul earthquake swarm (Reno, Nevada): interplay of fluid and faulting. J. Geophys. Res. Solid Earth 121, 8196–8216.

Sáez, A., Lecampion, B., 2023. Post-injection aseismic slip as a mechanism for the delayed triggering of seismicity. Proc. R. Soc. A, 479 (2273), 20220810.

Sáez, A., Lecampion, B., Bhattacharya, P., Viesca, R.C., 2022. Three-dimensional fluid-driven stable frictional ruptures. J. Mech. Phys. Solids 160, 104754. https://doi.org/10.1016/j.jmps.2021.104754.

Schultz, R., Ellsworth, W.L., Beroza, G.C., 2023a. An ensemble approach to characterizing trailing-induced seismicity. Seismol. Soc. Am. 94, 699–707.

Schultz, R., Park, Y., Aguilar Suarez, A.L., Ellsworth, W.L., Beroza, G.C., 2023b. En echelon faults reactivated by wastewater disposal near Musreau Lake. Alberta. Geophys. J. Int. 235, 417–429. https://doi.org/10.1093/gji/ggad226.

Segall, P., 2010. Earthquake and Volcano Deformation. Princeton University Press. https://doi.org/10.1515/9781400833856.

Segall, P., Lu, S., 2015. Injection-induced seismicity: poroelastic and earthquake nucleation effects. J. Geophys. Res. Solid Earth 120, 5082–5103. https://doi.org/10.1002/2015JB012060.

Shapiro, S.A., Dinske, C., 2007. Violation of the Kaiser effect by hydraulic-fracturing-related microseismicity. J. Geophys. 4 (4), 378–383.

Shapiro, S.A., Huenges, E., Borm, G., 1997. Estimating the crust permeability from fluid-injection-induced seismic emission at the KTB site. Geophys. J. Int. 131, F15–F18.

Shelly, D.R., Taira, T., Prejean, S.G., Hill, D.P., Dreger, D.S., 2015. Fluid-faulting interactions: fracture-mesh and fault-valve behavior in the February 2014 Mammoth Mountain, California, earthquake swarm. Geophys. Res. Lett. 42, 5803–5812. https://doi.org/10.1002/2015GL064325.

Sibson, R.H., 1992. Fault-valve behavior and the hydrostatic-lithostatic fluid pressure interface. Earth Sci. Rev. 32, 141–144. https://doi.org/10.1016/0012-8252(92)90019-P.

Sirorattanakul, K., Ross, Z.E., Khoshmanesh, M., Cochran, E.S., Acosta, M., Avouac, J.P., 2022. The 2020 Westmorland, California earthquake swarm as aftershocks of a slow slip event sustained by fluid flow. J. Geophys. Res. Solid Earth 127, e2022JB024693. https://doi.org/10.1029/2022JB024693.

Talwani, P., Chen, L., Gahalaut, K., 2007. Seismogenic permeability, ks. J. Geophys. Res. Solid Earth 112. https://doi.org/10.1029/2006JB004665.

Valley, B., Evans, K.F., 2007. Stress state at Soultz-sous-Forêts to 5 km depth from wellbore failure and hydraulic observations. In: Proceedings of the 32nd Workshop on Geothermal Reservoir Engineering, p. 17481. –17469.

Vidale, J.E., Shearer, P.M., 2006. A survey of 71 earthquake bursts across southern California: exploring the role of pore fluid pressure fluctuations and aseismic slip as drivers. J. Geophys. Res. Solid Earth 111, B05312. https://doi.org/10.1029/2005JB004034.

Wang, T.A., Dunham, E.M., 2022. Hindcasting injection-induced aseismic slip and microseismicity at the cooper basin enhanced geothermal systems project. Sci. Rep. 12, 19481. https://doi.org/10.1038/s41598-022-23812-7.

Wassing, B.B.T., Candela, T., Osinga, S., Peters, E., Buijze, L., Fokker, P.A., Van Wees, J. D., 2021. Time-dependent seismic footprint of thermal loading for geothermal activities in fractured carbonate reservoirs. Front. Earth Sci. 9 https://doi.org/10.3389/feart.2021.685841.

Whidden, K.M., Petersen, G., Pankow, K.L., 2023. Seismic Monitoring of the 2022 Utah FORGE Stimulation: the View From the Surface. In: Proceedings of the 48th Workshop on Geothermal Reservoir Engineering. California. Stanford University.

Wibberley, C.A., 2002. Hydraulic diffusivity of fault gouge zones and implications for thermal pressurization during seismic slip. Earth Planets Space 54, 1153–1171.

Wynants-Morel, N., Cappa, F., De Barros, L., Ampuero, J.P., 2020. Stress perturbation from aseismic slip drives the seismic front during fluid injection in a permeable Fault. J. Geophys. Res. Solid Earth 125, e2019JB019179.

Yildirim, E.C., Im, K., Elsworth, D., 2020. The influence of fault reactivation on injection-induced dynamic triggering of permeability evolution. Geophys. J. Int. 223, 1481–1496. https://doi.org/10.1093/gji/ggaa382.

Yoshida, K., Hasegawa, A., 2018. Sendai-Okura earthquake swarm induced by the 2011 Tohoku-Oki earthquake in the stress shadow of NE Japan: detailed fault structure and hypocenter migration. Tectonophysics 733, 132–147. https://doi.org/10.1016/j.tecto.2017.12.031. Physics of Earthquake Rupture Propagation.

Zang, A., Oye, V., Jousset, P., Deichmann, N., Gritto, R., McGarr, A., Majer, E., Bruhn, D., 2014. Analysis of induced seismicity in geothermal reservoirs – An overview. Geothermics 52, 6–21. https://doi.org/10.1016/j.geothermics.2014.06.005. Analysis of Induced Seismicity in Geothermal Operations.